Prediction of Solar Irradiance One Hour Ahead Based on Quantum Long Short-Term Memory Network

YUNJUN YU[1] (Member, IEEE), **GUOPING HU[1], CAICHENG LIU[1],**
JUNJIE XIONG[2], AND ZIYANG WU[3]

[1]School of Information Engineering, Nanchang University, Nanchang 330031, China
[2]State Grid Jiangxi Electric Power Co. Ltd., Electric Power Research Institute, Nanchang 330031, China
[3]University of California Irvine, Irvine, CA 92697 USA

Corresponding author: Yunjun Yu (e-mail: yuyunjun@ncu.edu.cn).

ABSTRACT The short-term forecasting of photovoltaic (PV) power generation ensures the scheduling and dispatching of electrical power, helps design a PV-integrated energy management system, and enhances the security of grid operation. However, due to the randomness of solar energy, the output of the PV system will fluctuate, which will affect the safe operation of the grid. To solve this problem, a high-precision hybrid prediction model based on variational quantum circuit (VQC) and long short-term memory (LSTM) network is developed to predict solar irradiance 1 hour in advance. VQC is embedded in LSTM to iteratively optimize the weight parameters of four gates (forgetting gate, input gate, cell state, and output gate) to improve prediction accuracy. To evaluate the prediction performance of this model, five solar radiation observatories located in China are selected, together with widely used models including seasonal autoregressive integrated moving average, convolution neural network, recurrent neural network (RNN), gate recurrent unit, (GRU), and LSTM; comparisons are made under different seasons and months. The experimental results show that the annual average root mean square error of the quantum long short-term memory model is 61.756 W/m^2, which is reduced by 10.7%, 13.9%, 8.1%, 3.8%, and 3.4%, respectively, compared with other models; the annual average mean absolute error is 24.257 W/m^2, which is reduced by 28.1%, 28.9%, 24.1%, 12.2%, and 12.8%, respectively, compared with other models; the annual average R-Square (R^2) is 0.946, which is improved by 1.5%, 1.9%, 1.2%, 0.4%, and 0.4%, respectively, compared with other models.

INDEX TERMS Long short-term memory (LSTM) network, quantum neural network, solar irradiance forecasting, variational quantum circuit (VQC).

I. INTRODUCTION

Solar energy engineering is one of the energy alternatives for global sustainable development goals [1]. Photovoltaic (PV) panels are the biggest driving force in the rapid growth of solar power generation [2]. However, PV systems are susceptible to environmental factors such as sunlight, season, and geographic location, resulting in the PV characteristics of being stochastic, intermittent, and variable [3], [4]. These characteristics are required to reduce the efficiency of PV output [5]. The reliability and stability of the power supply connected to the main grid will also be affected [6], [7]. Reliable PV prediction can provide important data support for power system operation, which is the basis and key to realize the large-scale utilization of solar energy resources [8]. And it is very important for the safe and stable operation of the PV system.

Generally, PV prediction methods mainly focus on PV output and solar irradiance. In order to enable the prediction model to mine the inherent characteristics between the data, the deep analysis of a large number of historical PV or solar irradiance data is required [9]. A PV system is affected by environmental conditions and geographic location, which lead to a strong correlation between meteorological characteristics and PV output. Meteorological data can be obtained from local meteorological stations. In addition, global horizontal irradiance (GHI) in the next period of time can be obtained through the developed prediction model.

In the existing literature, the methods for solar irradiance prediction are mainly divided into three categories: physical model, statistical model, and machine learning (ML) model. The physical model utilizes mathematical equations to describe the physical state of meteorological conditions and the dynamic movement of the atmosphere, thereby, deriving the mathematical relationship between the physical state and solar irradiance [10]. In general, these models compute solar irradiance by the formulation of mathematical analysis of physical and dynamic atmospheric variables. The performance of these physical models highly depends on the climate and the dynamic solar irradiance of the particular target area, which makes it almost impossible to predict accurately. Moreover, these numerical models are more complicated and time consuming.

Compared with physical models, statistical models are designed to observe the changing trend of historical time-series data to find the mathematical relationship between historical solar irradiance and meteorological parameters. The statistical methods commonly used in solar irradiance prediction include autoregressive (AR) [11], autoregressive moving average, and autoregressive integrated moving average (ARIMA) [12]. Alsharif et al. [13] developed a seasonal autoregressive integrated moving average (SARIMA) model to predict the daily and monthly solar radiation in Seoul, South Korea, based on the hourly solar radiation data obtained from the Korean Meteorological Administration over 37 years (1981–2017). According to the findings, the expected average monthly solar radiation ranges from 176 to 377 Wh/m^2, which is compatible with the general trends of the highest and lowest monthly values and daily fluctuations. Basmadjian et al. [14] proposed a set of ARIMA-based models for each month of the year, and introduced exogenous variables for analysis. They designed different models for each month, which is an excellent method, and finally achieved an error of no more than 10%. Atique et al. [15] used the ARIMA model to forecast the total daily solar energy generated by a solar panel located in a research facility. The model was developed by using techniques like differencing, ACF, PACF, and ADF test, and was validated by using the Akaike information criterion and error sum of squares. This work can be used as a good building block for further research into forecasting of renewable energy generation. Basmadjian et al. [16] proposed a methodology to generate accurate predictions, which consists of two main phases. In the first phase, the most relevant variables having impact on the generation of the renewables were identified using correlation analysis. The second phase consists of 1) estimating model parameters, 2) optimizing and reducing the number of generated models, and 3) selecting the best model for the method under study. The average absolute error based on ARIMA, SARIMA, and SARIMA with exogenous factor (SARIMAX) models is between 6.76% and 11.57%. Vagropoulos et al. [17] compared four practical methods for electricity generation forecasting of grid-connected PV plants, namely, SARIMA, SARIMAX, modified SARIMA,

and artificial neural network (ANN)-based model. According to the results, the ANN models, the SARIMAX model, and the modified SARIMA model are superior in terms of the day-ahead forecasting performance compared to the persistence model (PM) and the SARIMA model. Eldali et al. [18] employed an ARIMA model and real data from ERCOT for demonstrating an improved wind power forecasts (WPFs) effectiveness and usability. The results show WPF improvements as vector norms of the relative error and how the error is reduced in all the cases. Generally, statistical models perform well in predicting future values of stationary solar irradiance time series. However, time-series data of solar irradiance show nonstationary behavior due to cloud and seasonal effects. As a result, these models cannot accurately capture fluctuations in data.

To overcome the drawbacks of statistical models, the data-driven-based ML algorithm was extensively used to predict solar irradiance and PV power. ML-based schemes can process the nonlinear relationship of meteorological data. For instance, Mellit et al. [19] proposed an ANN-multilayer perceptron architecture by using the Levenbeg–Marquardt backpropagation algorithm to predict solar irradiance based on 24-h ahead for the GCPV plant in Trieste, Italy. The input parameters applied were air temperature, daily solar irradiance, and day of the months. The simulation results demonstrated that the metric performances of correlation coefficient are 98% and 94% for sunny and cloudy days, respectively. Shi et al. [20] developed the PV power output prediction for 1-day ahead based on support vector machine and the features of weather categorization at a PV station in China. The historical model data were categorized into four classes of historical weather conditions, i.e., cloudy, sunny, rainy, and foggy. As a result, the sunny model was emerging as the best among the others in PV power forecasting, and the average forecasting errors of root mean square error (RMSE) and MRE are 2.10 MW and 8.64%, respectively. However, the conventional ML methods have limited intensive feature extraction of large amounts of diverse data, which is challenging to predict accurately in nonidentical distribution parameters.

In recent years, deep learning models have gained extensive attention as they perform well over conventional ML models due to the following reasons: they can extract features automatically with no or little knowledge of background details, their strong generalization power, and the ability to handle Big Data. A recurrent neural network (RNN) is a class of ANNs specially designed to model sequential or time-series data. Cao et al. [21] used the RNN model to predict the solar irradiance one day in advance. They used the data training model with a time interval of 1 h from 1995 to 2000, and finally obtains the RMSE value of 44.326 W/m^2. Aslam et al. [22] used RNN, gate recurrent unit (GRU), and long short-term memory (LSTM) to predict the solar irradiance one hour and one day in advance. The data used were the data of 10 years from 2007 to 2017, with a time interval of 1 h. In the prediction experiment one hour in advance,

RNN, GRU, and LSTM obtained RMSE values of 105.277, 99.722, and 108.888 W/m^2, respectively, and GRU shows the best prediction performance. In the prediction experiment one day in advance, RNN, GRU, and LSTM obtained RMSE values of 63.125, 55.821, and 55.277 W/m^2, respectively, and LSTM shows the best prediction performance. Both LSTM and GRU are variants of RNN model, and the difference between them is not big. The choice of which model depends on the specific task. In addition, Yu et al. [23] proposed a prediction model based on LSTM to predict solar radiation under complex weather conditions. They reported that the proposed LSTM model shows an RMSE in a range of 45.84 and 41.37 W/m^2 for the considered locations. Qing et al. [24] utilized the LSTM for GHI forecasting using weather forecast and meteorological data. The developed model shows a good accuracy over other considered models, with an RMSE value of 76.245 W/m^2. The independent LSTM model has a singularity and cannot perform all work effectively. The combined hybrid network model not only reduces the limitations of the independent model, but can also combine multiple models to achieve a more comprehensive execution of the prediction task [25]. Therefore, some researchers combined LSTM and other models to extract features from the data to improve the accuracy of time-series forecasting. Zhang et al. [26] introduced a hybrid forecasting model with a combination of autoencoder LSTM (AE-LSTM) and PM. The robustness of the deep learning model is boosted by AE-LSTM, which enhances the uncertainty estimation. Wang et al. [27] proposed a hybrid deep learning model LSTM–convolutional network and applied it to a PV power prediction. In the proposed hybrid model, the temporal features of the data are extracted first by the LSTM, and then, the spatial features of the data are extracted by the convolution neural network (CNN).

In addition, as quantum computers have made breakthroughs in computing scale and stability, ML based on quantum algorithms has attracted attention. Quantum machine learning (QML) has become a rapidly developing research direction. A number of studies used quantum technology to improve ML algorithms, which provide references for future QML research. Due to the emergence of noisy intermediate-scale quantum (NISQ) [28] machines, the VQC algorithm [29], [30], [31], [32] has become the main candidate for finding a shallow quantum algorithm that surpasses the classical computer. By taking advantage of quantum computing with much fewer parameters [33], the VQC on NISQ has successfully implemented classical classification and clustering algorithms on benchmark datasets [34]. Chen et al. [35] explored VQC for deep reinforcement learning, which uses low-depth shallow VQC to reshape each module of the model, such as experience playback and target networks. Giani et al. [36] pointed out that there is a disconnect between quantum computing and practical applications, so it is necessary to find out relevant application fields to prove the potential of quantum computing to solve problems. They believe that the expansion of renewable energy will bring many new challenges to the power grid, so quantum computing will play an important role in the field of renewable energy. They also recommend potentially fruitful areas of crossover research to advance applications of quantum computing and renewable energy. Estimates from the New England grid operator (ISO-NE) suggest potential savings in the tens of millions of dollars for reducing the error of solar forecasting [37], [38]. Solar irradiance forecasting, wind-blades interactions, and hydrodynamics follow the viscous fluid physical law and obey the Navier–Stokes nonlinear partial differential equations. This is a new application area for quantum computing, and we have already seen initial studies using both the gate model [39], [40], [41] and annealing [42].

Inspired by the VQC, this work proposed a novel hybrid quantum long short term memory (QLSTM) model architecture, which embeds the VQC into the LSTM. Then input the meteorological data sequence into the QLSTM model to test its ability to predict short-term solar irradiance. The main contributions of this study can be summarized as follows. 1) We extend the classical LSTM to the quantum field, and replace the classical neural network in the LSTM cell with VQCs, which would play the role of feature extraction and data compression. We then applied the QLSTM model to the field of solar energy prediction, which provides a reference for the application of quantum computing in the field of renewable energy. 2) We compare the QLSTM model with the commonly used SARIMA, CNN, RNN, GRU, and LSTM models under different experimental conditions. The results show that the overall performance of the QLSTM model is better than these baseline models. This shows that quantum computing has a very broad application prospect in the field of renewable energy.

The rest of this article is organized as follows. Section II introduces the structure of QLSTM. Section III presents data preprocessing. The experimental results are presented and analyzed in Section IV. Finally, Section V concludes this article.

II. QLSTM MODEL
A. VARIATIONAL QUANTUM CIRCUIT
A variational quantum circuit (VQC) is a quantum circuit with adjustable parameters optimized iteratively. The main function of the VQC circuit is feature extraction and data compression. Its generic structure is shown in Fig. 1. The VQC consists of three parts: data encoding layer (with R_x), variational layer, and quantum measurement layer. The encoding module first encodes the data information into the quantum state of qubit, and then, the gate operation of the entanglement module contains trainable weights. The evolved quantum state is measured to derive the classical output.

1) DATA ENCODING LAYER
A quantum embedding represents classical data as quantum states in a Hilbert space via a quantum feature map. It takes a classical datapoint x and translates it into a set of gate
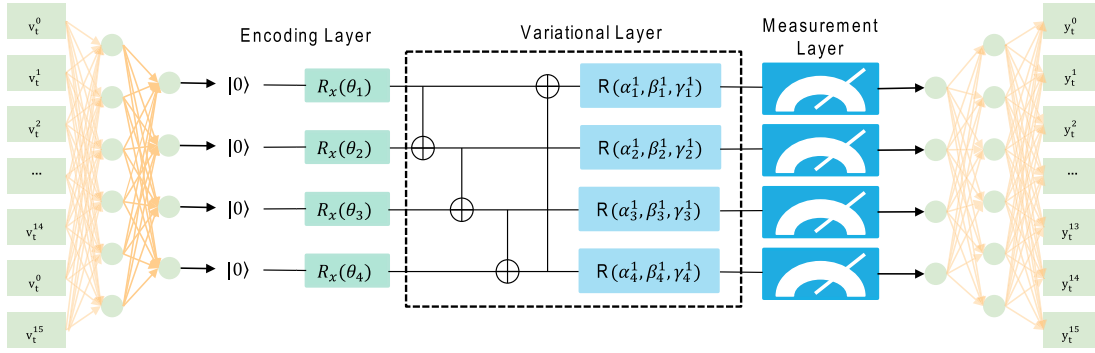
FIGURE 1. Generic VQC architecture for QLSTM. It consists of three layers: the data encoding layer, the variational layer, and the quantum measurement layer. Note that the number of qubits can be adjusted to the problem of interest.

parameters in a quantum circuit, creating a quantum state $|\psi_x\rangle$.

In the amplitude-embedding technique, data are encoded into the amplitudes of a quantum state. A normalized classical N-dimensional datapoint x is represented by the amplitudes of an n-qubit quantum state $|\psi_x\rangle$ as

$$|\psi_x\rangle = \sum_{i=1}^{N} x_i * |i\rangle \qquad (1)$$

where $N = 2^n$, x is the ith element of x, and $|i\rangle$ is the ith computational basis state.

2) VARIATIONAL LAYER

After the classical state data encoded into a quantum state, it is passed to the variable layer. The variant layer is represented by a dashed box in Fig. 1. After the data enter the variant layer, a number of entanglement operations are performed. These entanglement operations are composed of several controlled NOT (CNOT) gates and single-qubit rotation gates. CNOT gates are used for each pair of qubits with fixed adjacency of 1 and 2 (in a cyclic manner) to produce multiqubit entanglement. The single-qubit rotation gates with three parameters is shown as follows:

$$R(\alpha_i{}^j, \beta_i{}^j, \gamma_i{}^j) = R_x(\alpha_i{}^j)R_y(\beta_i{}^j)R_z(\gamma_i{}^j) \qquad (2)$$

where parameters α_i^j, β_i^j, and γ_i^j are the parameters for the iterative optimization of the VQC.

3) QUANTUM MEASUREMENT LAYER

Behind the variable layer is the quantum measurement layer. On the basis of calculation, the expected value of each qubit is obtained through Pauli matrix σ_Z as shown in (3). The expectation values of each qubit can be computed using classical computers through the utilization of PennyLane, which is a quantum simulation software. After a series of quantum entanglement operations, the measured VQC output is a fixed-length classical vector. In the proposed QLSTM, the measured values from each of the VQC will be processed
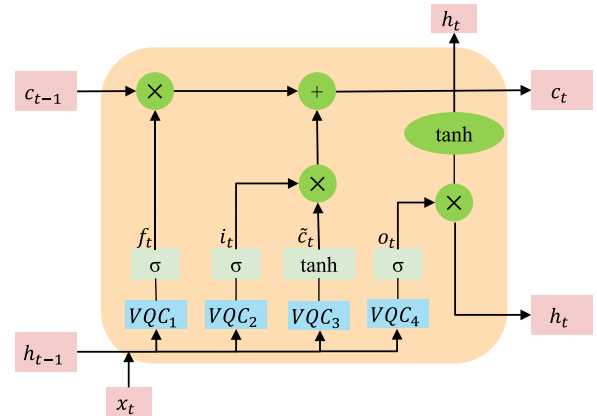

FIGURE 2. Architecture of QLSTM. Each VQC box is of the form as detailed in Fig. 1. The σ and tanh blocks represent the sigmoid and the hyperbolic tangent activation function, respectively. x_t is the input at time t, h_t is for the hidden state, c_t is for the cell state. VQC_1 represents the forget gate, deciding if the input should be added to memory. The VQC_2 and VQC_3 represent the update gates, updating the cell memory if there is need. The VQC_4 represents the output gate, outputting the result.

within a QLSTM cell

$$\sigma_Z = \begin{bmatrix} 1 & 0 \\ 0 & -1 \end{bmatrix}. \qquad (3)$$

B. QLSTM NETWORK

There are four VQCs in a QLSTM unit, as shown in Fig. 2. From VQC_1 to VQC_4, the input is the concatenation v_t of the x_t from the current time step, and h_{t-1} from the previous time step, the output is a vector obtained from the quantum measurement layer. The measured values, which are Pauli Z expectation values of each qubit by design, then go through nonlinear activation functions (sigmoid and tanh). The four VQCs are the same, each of them are defined by a basic VQC from Fig. 1. The VQC includes a trainable fully connected layer that squeezes the dimensional space of the information down to the circuit size of the VQC. After each VQC, a quantum measurement of the expectation for each wire is fed to the trainable fully connected expansion layer. The expansion layer increases the size from the quantum circuit back to the

TABLE 1. Meteorological Variables and Value Range

City	GHI (W/m^2)	Cloud type	Dew point (°C)	Temperature (°C)	Relative humidity (%)	Solar zenith angle (degree)	Pressure (mbar)	Wind speed (m/s)
Urumqi	0∼1019	0∼9	-33.4∼16.1	-24.8∼36.5	10.22∼92.65	20.35∼159.72	857∼887	0.1∼10.1
Hohhot	0∼1036	0∼9	-36.9∼22.3	-27.3∼38.8	7.34∼100	18.16∼161.67	878∼911	0.1∼14
Harbin	0∼975	0∼9	-37.3∼28.1	-33.3∼38.1	13.3∼100	22.95∼156.91	969∼1026	0.1∼12
Wuhan	0∼1016	0∼9	-17.4∼29.8	-9.8∼39.8	16.91∼100	8.94∼171.65	990∼1044	0∼10.9
Haikou	0∼1038	0∼9	5.8∼28.7	10.4∼33.9	41.69∼100	3.52∼177.63	997∼1038	0.1∼9.9
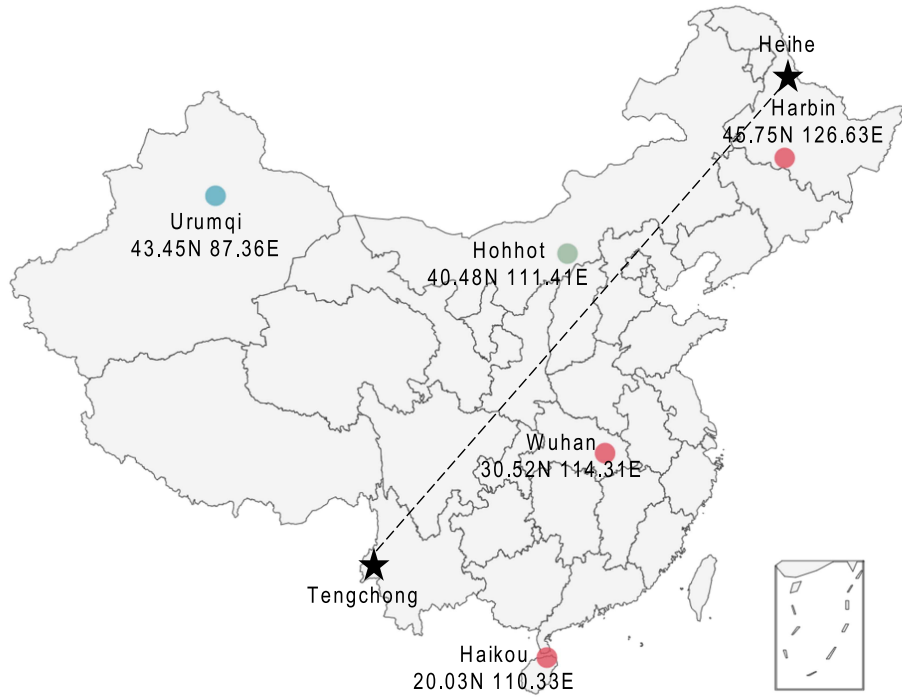
FIGURE 3. Coordinates of the studied cities. The figure shows the longitude and latitude of the five cities and their geographical positions on the map. In addition, the Heihe–Tengchong line is the boundary line of physical geography. Basically, it is consistent with the 400 mm precipitation line of China, and the geographical and climatic conditions on both sides are also very different.

required dimensional space of the classic network. This is then processed using classical LSTM approaches.

The QLSTM architecture can be defined as follows:

$$f_t = \sigma(\text{VQC}_1(v_t)) \tag{4}$$

$$i_t = \sigma(\text{VQC}_2(v_t)) \tag{5}$$

$$\widetilde{c}_t = \tanh(\text{VQC}_3(v_t)) \tag{6}$$

$$c_t = f_t \times c_{t-1} + i_t \times \widetilde{c}_t \tag{7}$$

$$o_t = \sigma(\text{VQC}_4(v_t)) \tag{8}$$

$$h_t = o_t \times \tanh(c_t). \tag{9}$$

III. DATA PREPROCESSING

A. DATA DESCRIPTION

Climate type and geographical location are decisive factors for the distribution and availability of GHI in an area. Download the solar irradiance data and meteorological data of five cities in China from the US National Solar Radiation Data Base. The dataset consists of eight weather variables: solar radiation, temperature, pressure, relative humidity, wind speed, cloud type, dew point, and solar zenith angle. The meteorological variables and value range are shown in Table 1. The data are gathered from 1 January 2016 to 31 December 2019. Notably, each meteorological variable has a major or minor impact on solar irradiance. The coordinates of the five cities are shown in Fig. 3. Five cities belong to four climate types, including temperate continental climate, temperate monsoon climate, subtropical monsoon climate, and tropical monsoon climate.

The daily GHI distribution of the five studied cities in each month from 2016 to 2019 are shown in Fig. 4 by the form of box diagrams, and the information on the studied cities is shown in Table 2. The purpose is to observe and filter anomalous data, as shown by the small orange dots in Fig. 4. For the abnormal data, we use the mean value correct method to process it, that is, use the average value of consecutive observations to correct the outlier. It can be seen intuitively that the median distribution of GHI in Urumqi, Hohhot, and Harbin gradually rises from January to June and descends from July to December. From the median distribution diagram of Wuhan, it can be observed that it increases gradually from January to July, and then decreases gradually
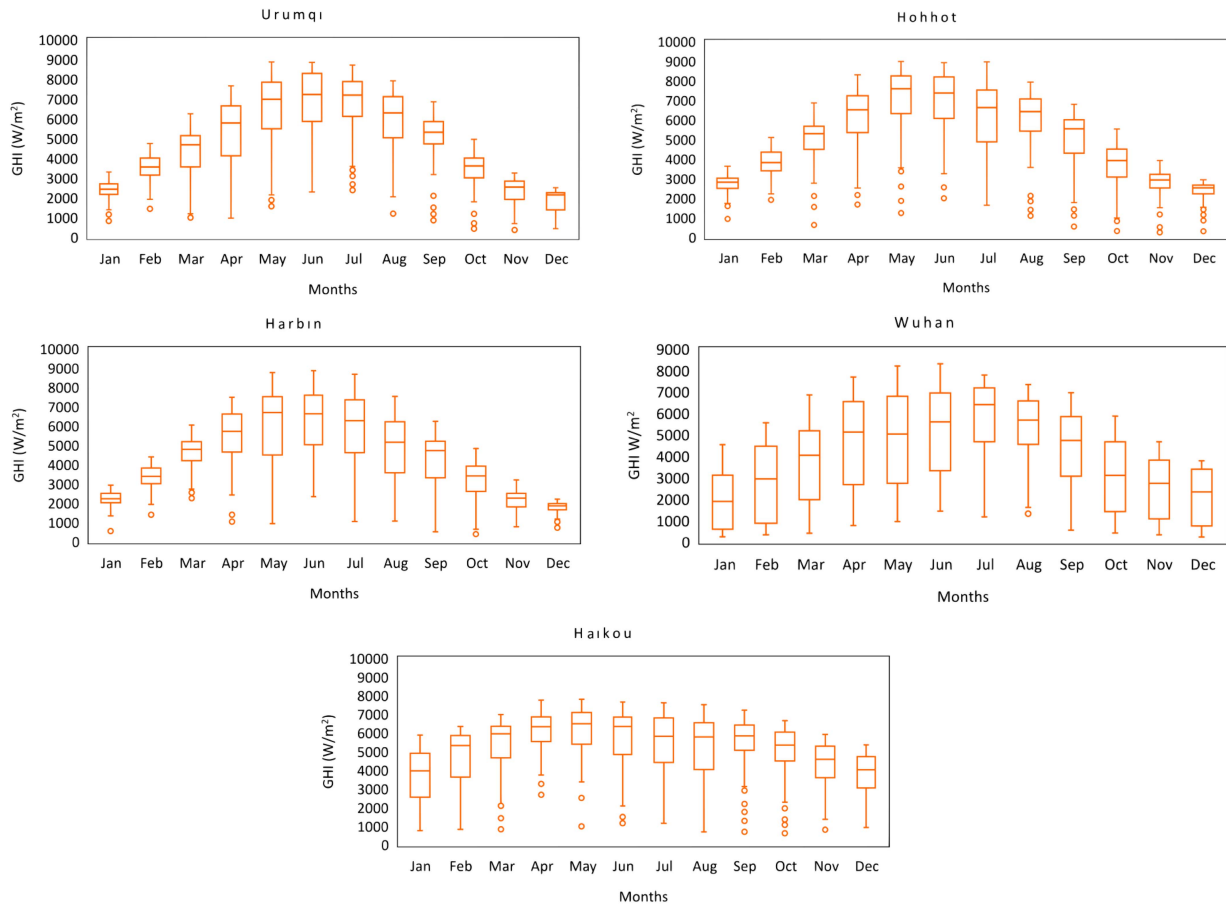
FIGURE 4. Distribution of daily GHI in each month from 2016 to 2019. Box chart is used to reflect the original distribution of solar irradiance data, in which small dots represent abnormal values.

TABLE 2. Information of the Studied Cities

City	Coordinates	Altitude	Climate	Average temperature	Average humidity	Daily sunshine hour
Urumqi	43.64N, 87.45E	1270 m	Temperate continental climate	7 °C	58%	7.58 h
Hohhot	40.84N, 111.69E	1073 m	Temperate continental climate	8 °C	49%	7.2 h
Harbin	45.84N, 126.65E	117 m	Temperate monsoon climate	4.2 °C	65%	6.25 h
Wuhan	30.62N, 114.31E	31 m	Subtropical monsoon climate	17.1 °C	72%	4.77 h
Haikou	20.08N, 110.37E	1 m	Tropical monsoon climate	24 °C	84%	5.5 h

from August to December. The median distribution of GHI is similar convex smooth curves for Urumqi, Hohhot, Harbin, and Wuhan, but the curve of Haikou is not smooth.

From the geographical point of view, the five locations can be described as follows. The Heihe–Tengchong line [43] is the dividing line of China's population density, which describes the macro pattern of population distribution in China with more in the East and less in the West. Urumqi and Hohhot above the line belong to low population density cities, and Harbin, Wuhan, and Haikou belong to high population density cities, which are below the line. Urumqi is located in Northwest China, which is deep inland and far away from the sea. It is surrounded by mountains on three sides and the northern plain is open. The ocean air flow is not easy to reach, forming an obvious temperate continental climate. Throughout the year, Urumqi has been mainly affected by

the northwest air flow from the inland of Asia, with sufficient sunshine time and less precipitation (annual precipitation is 310.8 mm). Hohhot is located in the northern part of China, in the midtemperate inland area. The Daqingshan Mountain in the north is a mountainous terrain, and the Tumochuan plain in the south. The terrain gradually slopes from north to south. Hohhot has a temperate continental climate. In spring and summer, it is dry and windy, with drastic changes in cold and warm. In autumn and winter, it is cold and dry, with plenty of sunshine. In addition, the annual precipitation is low (335.2–534.6 mm), and the precipitation is mainly distributed between July and August. Harbin is located in northeastern China, with the Zhangguangcailing branch hills in the southeast, the Xiaoxing'an Mountains in the north, and the Songhua River in the middle. The climate of Harbin is a midtemperate continental monsoon climate. The winter is
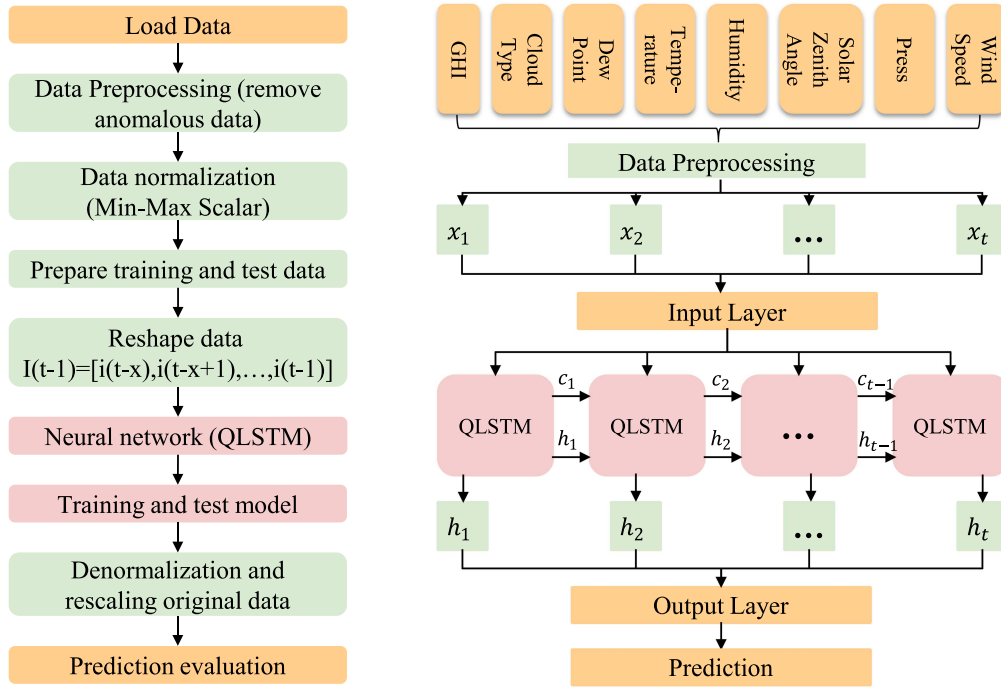
FIGURE 5. GHI prediction framework based on the QLSTM model. The figure on the left shows the general process of solar energy prediction, and the figure on the right shows some details of the corresponding parts.

mainly affected by the northeast monsoon, and it is cold and long. In summer, it is mainly affected by the Pacific Ocean's westward stretch from the north to the southwest, and the formed convective clouds will produce precipitation. The annual average precipitation is 569.1 mm, and the precipitation is mainly concentrated in June–September. Wuhan is located in central China, which is located in the east of the Jianghan Plain and the middle reaches of the Yangtze River. Wuhan has a north subtropical monsoon climate, with the characteristics of abundant rainfall, sufficient heat, cold winter, and hot summer, and four distinct seasons. In Wuhan, the convective cloud is caused by the intersection of the warm and humid air from the southwest and the cold air from the north. This has resulted in sufficient rainfall throughout the year in Wuhan, with annual precipitation ranging from 1150 to 1450 mm. Haikou is located in the south of China, with most of the mountains and hills in the south. Haikou is located in southern China and has a tropical monsoon climate. When the northeast monsoon and typhoon blow inland, topographic clouds are formed in Haikou as the topography rises. It has resulted in abundant rainfall in the region, with an average annual rainfall of 2067 mm, which is mainly distributed in summer and autumn. Mountains (orographic clouds), lakes, and seas (convective clouds) are the main topographic factors for the formation of regional clouds in the target city.

B. DATA DIVISION AND STANDARDIZATION

To utilize the deep learning technique for solar forecasting, the collected data are divided into a training set (2016–2018) and testing set (2019). As the scale of the retrieved data is inconsistent, this may influence the accuracy of the prediction.

Thus, the input time series is normalized according to the Min-Max method and converted to [0,1]. In addition, the denormalization of data is also achieved through the Min-Max method. The calculation method is as follows:

$$X_{\mathrm{norm}} = \frac{X - X_{\min}}{X_{\max} - X_{\min}} \qquad (10)$$

where X_{norm}, X, $X_{\min}$, and $X_{\max}$ is the normalized, original, minimum, and maximum input values.

The solar irradiance prediction framework based on QLSTM is shown in Fig. 5. As can be seen from Fig. 5, the collected data are preprocessed first and then input to the input layer. After passing through the input layer, the data are input into QLSTM, and then passed through the output layer, and finally, the predicted value is obtained. Hence, this is a quantum-classical hybrid approach. For each QLSTM block, its details are shown in Fig. 2. In each QLSTM block, the first sigmoid activation is known as the forget gate that is used to decide whether to update context c_t to include the new input. After the sigmoid, the result is multiplied onto c_{t-1}. The second sigmoid and the tanh activations are known as the input gates that are used to write the new input into the context. The result of the sigmoid and tanh activations is multiplied to either be added to c_{t-1}, or to ensure that the input is not added to c_{t-1}. The last sigmoid activation is known as the output gate where the actual prediction is performed. This output is also used to update the hidden layer h_t.

C. PARAMETERS DESIGN OF DEVELOPED MODEL

In this study, the developed model is based on Python 3.7, PennyLane software package, TensorFlow 2.0, and Keras 2.3.1 framework. In addition to the fully connected layer, the rectified linear unit [44] is selected as the activation function in all layers. In order to reduce the possibility of overfitting, the regularization method of dropout [45] is applied in each training batch, which ignores a few neurons with a certain probability. The hyperparameters of the model include the dropout value, batch size, and epoch. Their values are optimized by the grid search algorithm and are ultimately set to 0.1, 256, and 150, respectively. Mean absolute error (MAE) is selected as the loss function to measure the approximation between the predicted value P_f and actual value P_a. Adam (Adaptive moment estimation) [46] is selected as the optimizer, which is founded on the training data iteratively to update the neural network weights. The output obtained from the fully connected layer of the prediction model will be denormalized to obtain the true prediction GHI values after the model completed the prediction.

D. MODEL PERFORMANCE METRICS

As all the models are dealing with a regression problem, the quality of predictive accuracy of each model is evaluated through three basic error metrics, such as RMSE, MAE, and R-Square (R^2), which are widely used for predictive analysis.

RMSE: It is used to measure the standard deviation between the predicted GHI and the actual GHI as follows:

$$\text{RMSE} = \sqrt{\frac{N}{\sum_{i=1}^{N} \left(P_f - P_a \right)^2}}. \tag{11}$$

MAE: It can be explained as the average of absolute error value between the predicted GHI and the actual GHI. It is defined as follows:

$$\text{MAE} = \frac{\sum_{i=1}^{N} \left| P_f - P_a \right|}{N}. \tag{12}$$

R^2: It determines the degree of correlation between predicted GHI and the actual GHI as shown below:

$$R^2 = 1 - \frac{\sum_{i=1}^{N} \left(P_f - P_a \right)^2}{\sum_{i=1}^{N} \left(\bar{P_a} - P_a \right)^2} \tag{13}$$

where N represents the total number of datasets. P_f and P_a is the predicted GHI and actual GHI, respectively.

E. PV SYSTEM

A PV system is shown in Fig. 6 . According to the Code for Design of Photovoltaic Power Plants, the PV power generation can be calculated according to the solar energy resources of the site
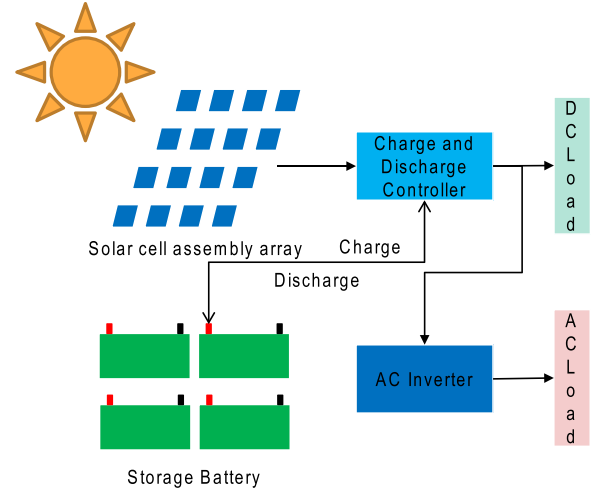
$$E_p = H_A * \frac{P_{AZ}}{E_S} * K \tag{14}$$

FIGURE 6. PV system.

where H_A represents the total solar radiation on the horizontal plane (kW · h/m^2, peak hours), E_P indicates the power generation (kW · h), E_S is the irradiance under standard conditions (constant=1 kW · h/m^2), $P_A Z$ represents the installed capacity of the module (kWp), and K represents the comprehensive efficiency coefficient (value 75%–85%).

IV. RESULTS AND DISCUSSION

This section is mainly about the experiments of the QLSTM model under different conditions and the analysis of the experimental results. The data are divided into a training set (2016–2018) and testing set (2019) with an interval of 1 h. To achieve solar irradiance prediction, the input given in all models consists of the meteorological information in the previous 24 h, and the output was the solar irradiance for the next hour. As all the models are dealing with a regression problem, the quality of predictive accuracy of each model is evaluated through three basic error metrics, such as RMSE, MAE, and R^2, which are widely used for predictive analysis. First, the annual prediction results of all models in five locations were analyzed. Second, in order to demonstrate the influence of seasonal changes on model predictions, the prediction performance of developmental model is calculated for four seasons (spring, summer, autumn, and winter). Finally, in order to explore the influence of different months on the prediction performance of the model, we evaluated the model performance under different months.

A. MODEL ANNUAL FORECAST PERFORMANCE EVALUATION

The experimental results of the solar irradiance prediction of each model are presented in Table 3, and the best evaluation values are indicated in bold. The experimental results show that the annual average RMSE of the QLSTM model is 61.756 W/m^2, compared with other models, it decreased by 10.7%, 13.9%, 8.1%, 3.8%, and 3.4%, respectively, the annual average MAE is 24.257W/m^2, which is reduced by
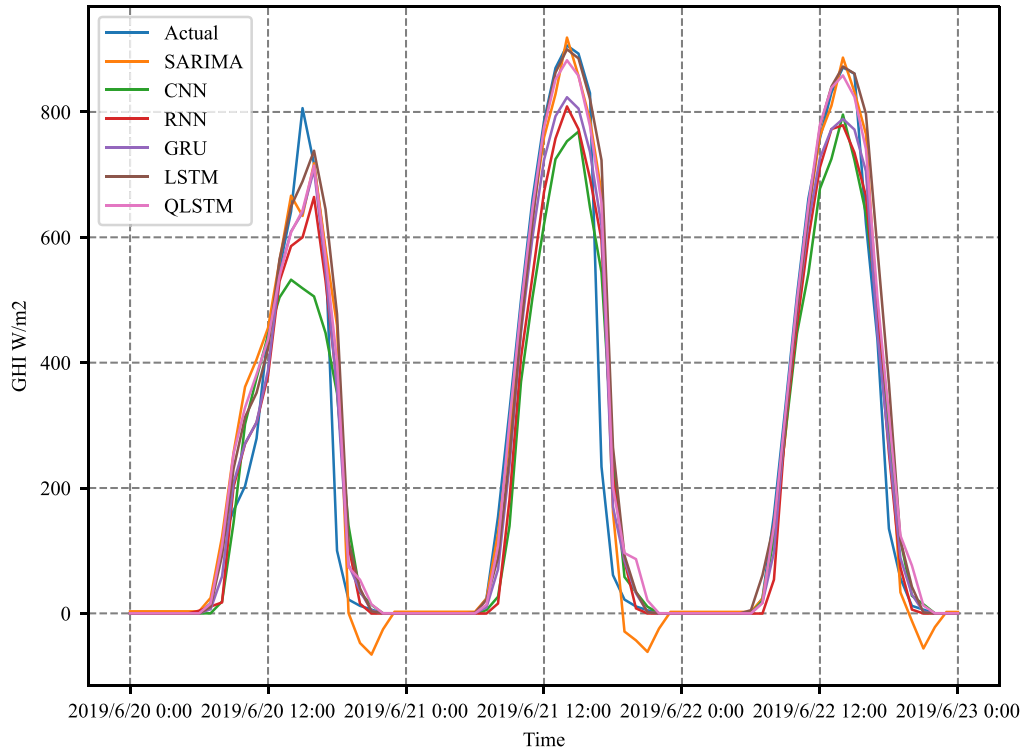
FIGURE 7. Prediction curve of six models in Urumqi from 20–22 June 2019.
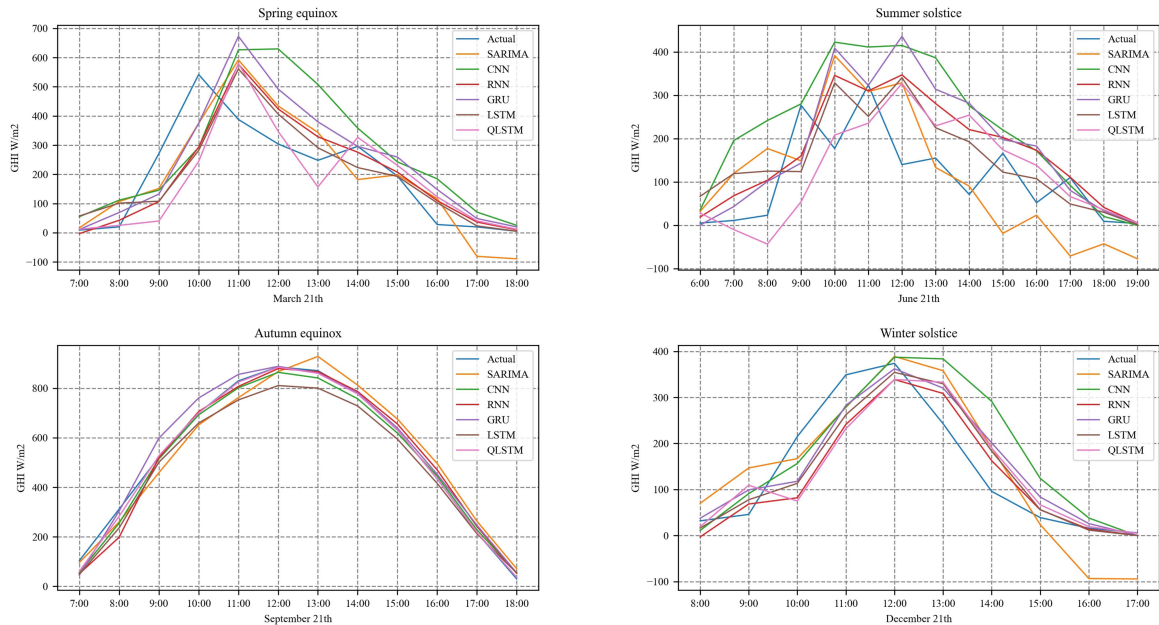

FIGURE 8. Prediction curves of the spring equinox, summer solstice, autumn equinox, and winter solstice of the six models in Wuhan.

28.1%, 28.9%, 24.1%, 12.2%, and 12.8%, respectively, and the annual average R^2 is 0.946, which is improved by 1.5%, 1.9%, 1.2%, 0.4%, and 0.4%, respectively. The observed values of solar irradiance were compared with the forecasted values in Urumqi, as shown in Fig. 7. It can be seen from Fig. 7 that the predicted value of QLSTM is almost consistent with the observed value curve.

As described in Section III-A, significant changes in model performance may be attributed to geographic and climatic differences in all studied cities. The bad performance at Haikou can be interpreted by the diversity climatic changes and topography of the region. Haikou is the southernmost capital city of China with the lowest dimension and the highest temperature. Haikou is close to the sea and the air
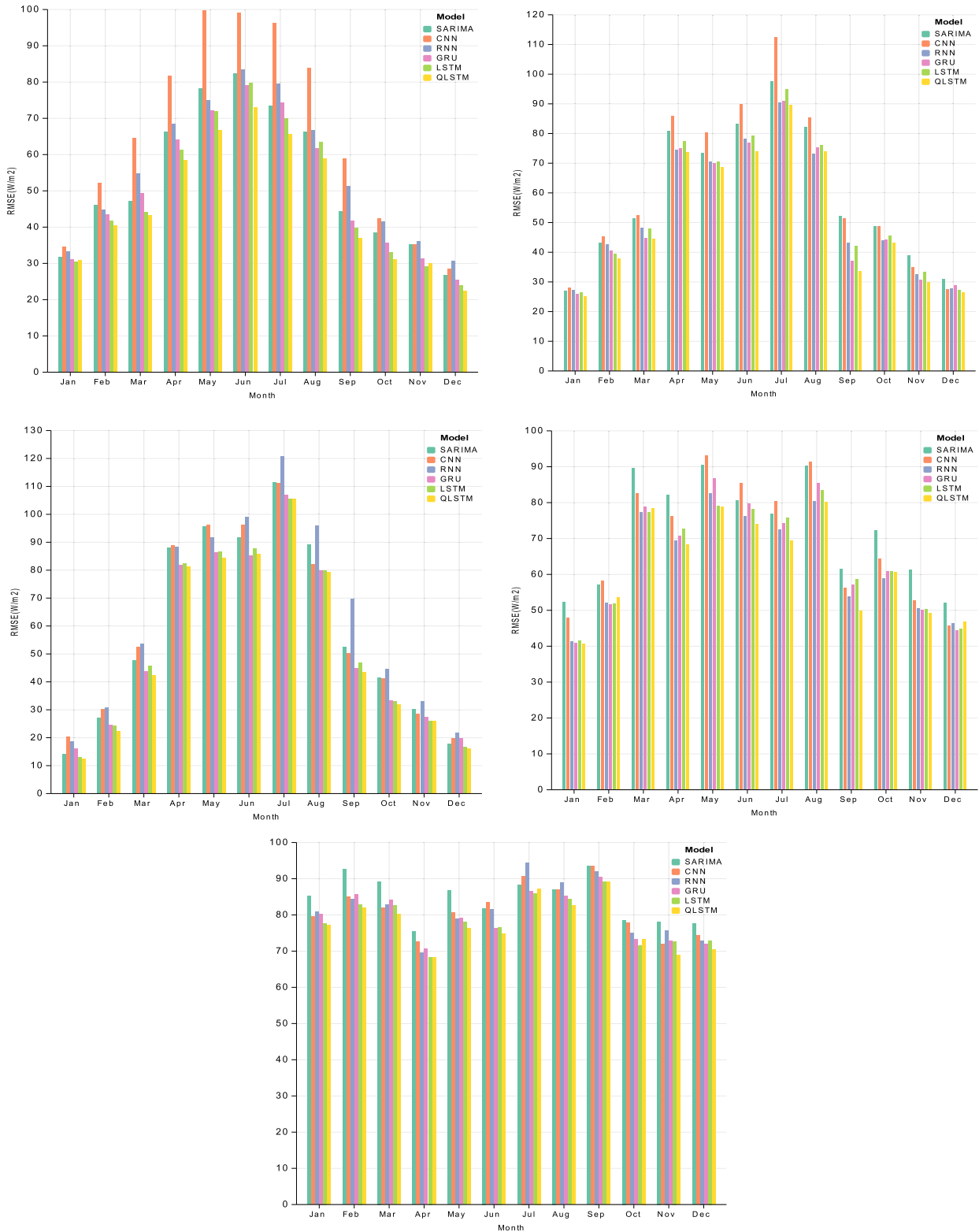
FIGURE 9. Comparison of the different model for each month by considering the RMSE performance metric.
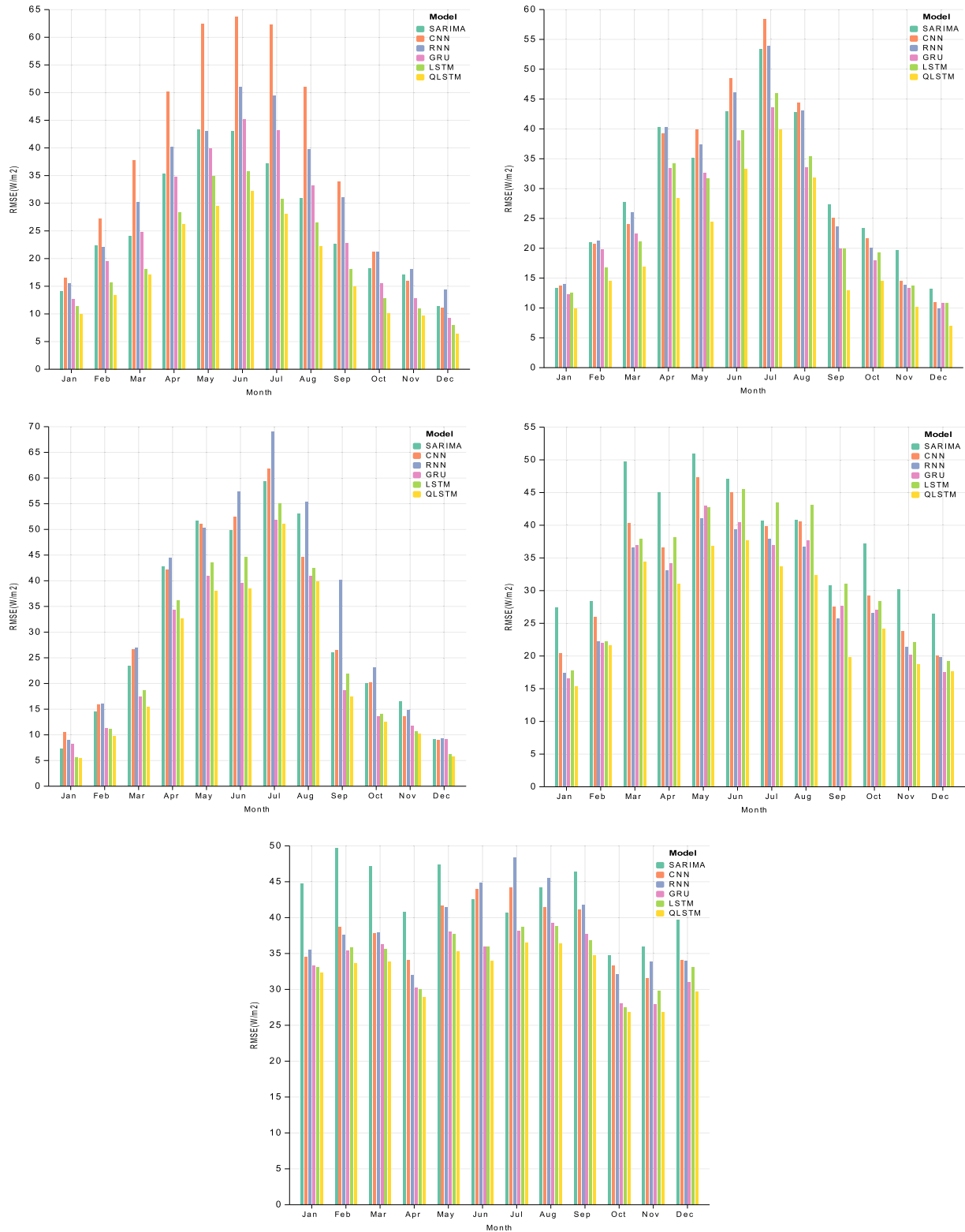
FIGURE 10. Comparison of the different model for each month by considering the MAE performance metric.

TABLE 3. Model Annual Prediction Performance Evaluation

City	Metric	SARIMA	CNN	RNN	GRU	LSTM	QLSTM
Urumqi	RMSE (W/m^2)	56.236	69.753	58.382	53.973	52.459	**49.361**
	MAE (W/m^2)	26.630	37.829	31.352	26.143	20.940	**18.313**
	R^2	0.957	0.933	0.953	0.960	0.962	**0.967**
Hohhot	RMSE (W/m^2)	63.303	67.459	58.258	57.674	59.454	**56.164**
	MAE (W/m^2)	30.050	30.246	24.948	22.609	25.154	**20.353**
	R^2	0.949	0.942	0.957	0.958	0.955	**0.960**
Harbin	RMSE (W/m^2)	67.730	67.948	72.364	62.380	62.571	**61.345**
	MAE (W/m^2)	31.272	31.306	34.733	24.909	25.918	**23.144**
	R^2	0.924	0.924	0.913	0.936	0.935	**0.938**
Wuhan	RMSE (W/m^2)	73.803	71.591	65.115	67.081	66.258	**64.110**
	MAE (W/m^2)	37.976	33.157	29.912	30.109	32.735	**27.037**
	R^2	0.916	0.921	0.935	0.931	0.933	**0.937**
Haikou	RMSE (W/m^2)	84.686	81.762	81.769	79.920	78.801	**77.800**
	MAE (W/m^2)	42.797	38.057	38.781	34.290	34.410	**32.436**
	R^2	0.913	0.919	0.919	0.923	0.925	**0.927**

humidity is relatively high. Therefore, it is easy to form clouds at high altitude, which affects the accuracy of the prediction model. In Wuhan, the southeast monsoon from the Indian Ocean and the South China Sea was blocked by the mountains at the junction of Hubei and Sichuan provinces, which lead to the rapid formation of convective and topographical clouds. This makes it particularly difficult for models to forecast. As for Harbin, which shows relatively bad performance, it is the northernmost metropolis with the highest latitude and lowest temperature in China. Harbin is affected by the Pacific southwest air flow in summer and controlled by the Mongolian northwest air flow in winter. This is the main reason for precipitation and snowfall, which is relatively difficult for models to predict. Due to its distance from the ocean, Hohhot and Urumqi are mainly affected by the northwest air flow rather than the marine monsoon. This causes convective clouds less in these two regions, and the prediction difficulty of the models is relatively small compared with the other three regions. As Urumqi is surrounded by mountains on three sides, it blocks part of the northwest airflow. The sky conditions of Urumqi are relatively stable than Hohhot, which lead to more accurate prediction results. In general, the QLSTM model has higher annual prediction performances than other comparable models, which proves that adding VQCs to LSTM has a positive effect of extracting the temporal correlation of data.

B. MODEL SEASONAL PREDICTION PERFORMANCE EVALUATION

Based on the annual performance, in this section, we study the influence of seasonal changes on model performance. The prediction results of the studied models for four seasons (spring, summer, autumn, and winter) in five cities are shown in Table 4. For each season, the best evaluation values obtained in all models are indicated in bold. According to the empirical results shown in the table, the proposed QLSTM achieved excellent results in terms of RMSE, MAE, and R^2. In general, our model shows a stable performance of all models in different seasons, among 60 sets (i.e., five sites, four seasons, and three performance metrics) of results achieved

the best performance in 58 groups. Furthermore, the solar prediction ability of QLSTM is slightly better than LSTM because QLSTM embeds VQC in LSTM, which enables LSTM to obtain more abundant features when processing memory information.

Besides, in order to better visualize the performance of the proposed QLSTM model and other comparable models, taking Wuhan as an example, we plotted the prediction curves of representative dates in four seasons, as shown in Fig. 8. It can be seen from Fig. 8 that the QLSTM proposed by us can fit the observed values well. Wuhan has a north subtropical monsoon climate with abundant rainfall, sufficient heat, rain, and heat in the same season, light and heat in the same season, cold in winter and hot in summer, and four distinct seasons. The prediction curve is consistent with the climatic characteristics of Wuhan.

C. MODEL PREDICTION PERFORMANCE EVALUATION UNDER DIFFERENT MONTHS

Moreover, the month prediction error of the GHI model in Table 5 was calculated to explore the impact of month alternation on the prediction results. The evaluation values of developed models for 12 months from January to December in all cities was given in Table 5, where the evaluation metrics marked in bold are equivalent to the best prediction performance. The results in Table 5 demonstrate the proposed hybrid QLSTM model shows the highest prediction accuracy in 50 of 60 cases (five cities, 12 months, and the metric of R^2). The prediction performance of QLSTM model outperforms other developed models in each month in Hohhot. For Urumqi, only in January and November, the QLSTM model did not get the highest R^2, and in other months, it got the highest R^2. For Harbin, QLSTM achieved the highest R^2 in 10 months, and LSTM achieved the highest R^2 in two months, which shows that the prediction performance of QLSTM is better than that of LSTM. In Wuhan, the QLSTM model achieved the highest R^2 in eight months, LSTM achieved in one, GRU achieved in two, and RNN achieved in three. Compared with SARIMA and CNN models, RNN series and

TABLE 4. Model Prediction Performance Evaluation in Different Seasons

City	Model	Spring			Summer			Autumn			Winter		
		RMSE	MAE	R^2	RMSE	MAE	R^2	RMSE	MAE	R^2	RMSE	MAE	R^2
Urumqi	SARIMA	65.227	34.229	0.950	74.246	36.968	0.949	39.581	19.282	0.969	35.461	15.725	0.958
	CNN	83.327	50.106	0.918	93.286	58.958	0.920	46.588	23.699	0.957	39.302	17.967	0.949
	RNN	66.582	37.764	0.948	76.897	46.692	0.945	43.472	23.436	0.962	36.556	17.122	0.956
	GRU	62.648	33.158	0.954	72.043	40.474	0.952	36.560	16.977	0.973	33.841	13.589	0.962
	LSTM	60.221	27.068	0.957	71.276	30.952	0.953	34.411	13.946	0.976	32.604	11.514	0.965
	QLSTM	**57.065**	**24.224**	**0.962**	**66.021**	**27.442**	**0.960**	**32.784**	**11.535**	**0.979**	**31.786**	**9.790**	**0.967**
Hohhot	SARIMA	69.559	34.335	0.953	87.990	46.390	0.924	46.946	23.431	0.961	34.104	15.659	0.967
	CNN	74.220	34.542	0.947	96.697	50.484	0.908	45.604	20.524	0.964	34.114	14.999	0.967
	RNN	65.287	29.551	0.959	80.858	38.632	0.936	40.253	17.128	0.972	32.952	14.163	0.970
	GRU	64.509	25.641	0.960	81.362	37.215	0.935	37.834	14.606	0.975	31.962	12.670	0.971
	LSTM	66.369	29.071	0.958	83.814	40.475	0.931	40.650	17.623	0.971	31.319	13.102	0.972
	QLSTM	**63.299**	**23.225**	**0.961**	**79.627**	**35.010**	**0.938**	**36.103**	**12.557**	**0.977**	**29.966**	**10.315**	**0.975**
Harbin	SARIMA	79.958	39.311	0.922	98.143	54.161	0.874	42.393	20.875	0.962	20.145	10.169	0.984
	CNN	81.444	39.967	0.919	97.281	52.995	0.876	41.092	20.081	0.964	23.723	11.633	0.977
	RNN	79.719	40.512	0.923	106.036	60.601	0.853	51.357	25.943	0.944	24.099	11.270	0.977
	GRU	73.150	30.886	0.935	91.638	44.160	0.890	35.982	14.624	0.972	20.447	9.518	0.983
	LSTM	73.919	32.706	0.933	91.773	47.406	0.890	36.416	15.494	0.972	18.496	7.552	0.986
	QLSTM	**71.901**	**28.636**	**0.937**	**91.005**	**43.159**	**0.891**	**34.611**	**13.413**	**0.975**	**17.326**	**6.908**	**0.988**
Wuhan	SARIMA	87.616	48.627	0.895	82.900	42.803	0.925	65.383	32.807	0.928	53.812	27.382	0.856
	CNN	84.358	41.519	0.903	85.842	41.827	0.920	58.098	26.915	0.943	50.654	22.058	0.873
	RNN	76.768	36.948	0.920	76.448	38.004	0.937	54.628	24.636	0.950	46.686	19.782	0.892
	GRU	79.186	38.123	0.914	80.002	38.376	0.931	56.274	25.015	0.947	**45.773**	18.616	**0.896**
	LSTM	76.558	39.672	0.920	79.266	44.029	0.932	56.832	27.209	0.946	46.095	19.686	0.894
	QLSTM	**75.520**	**34.148**	**0.922**	**74.691**	**34.577**	**0.940**	**53.652**	**20.995**	**0.952**	47.175	**18.168**	0.889
Haikou	SARIMA	84.107	45.166	0.923	85.804	42.481	0.925	83.656	39.002	0.915	85.157	44.538	0.863
	CNN	78.515	37.902	0.933	87.116	43.217	0.922	81.536	35.315	0.920	79.560	35.713	0.881
	RNN	77.425	37.177	0.935	88.552	46.292	0.920	81.257	35.889	0.920	79.353	35.666	0.881
	GRU	78.233	34.906	0.933	82.928	37.804	0.930	79.163	31.240	0.924	79.253	33.150	0.882
	LSTM	76.680	34.500	0.936	82.457	37.836	0.930	78.118	31.310	0.926	77.799	33.950	0.886
	QLSTM	**75.169**	**32.745**	**0.938**	**81.802**	**35.677**	**0.931**	**77.563**	**29.432**	**0.927**	**76.476**	**31.847**	**0.890**

TABLE 5. Comparison of the Different Model for Each Month by Considering the R^2 Performance Metric

City	Model	R^2											
		Jan	Feb	Mar	Apr	May	Jun	Jul	Aug	Sep	Oct	Nov	Dec
Urumqi	SARIMA	0.961	0.954	0.969	0.947	0.938	0.939	0.953	0.955	0.973	0.967	0.953	0.962
	CNN	0.954	0.940	0.942	0.919	0.900	0.912	0.919	0.928	0.953	0.960	0.953	0.957
	RNN	0.957	0.956	0.958	0.943	0.943	0.938	0.945	0.954	0.964	0.962	0.950	0.950
	GRU	0.963	0.959	0.966	0.950	0.947	0.944	0.952	0.961	0.976	0.972	0.963	0.966
	LSTM	**0.964**	0.962	0.973	0.955	0.948	0.943	0.958	0.959	0.978	0.976	**0.968**	0.970
	QLSTM	0.963	**0.964**	**0.974**	**0.959**	**0.955**	**0.952**	**0.962**	**0.965**	**0.982**	**0.979**	0.966	**0.973**
Hohhot	SARIMA	0.975	0.963	0.967	0.931	0.959	0.938	0.900	0.931	0.967	0.956	0.951	0.965
	CNN	0.973	0.960	0.966	0.922	0.951	0.928	0.867	0.926	0.968	0.956	0.961	0.972
	RNN	0.975	0.964	0.971	0.942	0.962	0.946	0.914	0.946	0.977	0.964	0.966	0.972
	GRU	0.977	0.968	0.975	0.941	0.962	0.948	0.913	0.942	0.983	0.963	0.970	0.969
	LSTM	0.976	0.969	0.972	0.937	0.962	0.944	0.905	0.941	0.978	0.961	0.964	0.972
	QLSTM	**0.979**	**0.972**	**0.976**	**0.943**	**0.964**	**0.951**	**0.915**	**0.944**	**0.986**	**0.965**	**0.971**	**0.974**
Harbin	SARIMA	0.991	0.980	0.966	0.914	0.896	0.912	0.842	0.841	0.961	0.959	0.961	0.979
	CNN	0.981	0.975	0.959	0.912	0.894	0.903	0.843	0.865	0.964	0.959	0.965	0.975
	RNN	0.984	0.974	0.957	0.913	0.905	0.898	0.814	0.816	0.931	0.952	0.953	0.969
	GRU	0.988	0.983	0.971	0.926	0.915	**0.924**	0.854	0.872	0.971	0.973	0.968	0.974
	LSTM	0.992	0.984	0.969	0.924	0.914	0.919	**0.859**	0.873	0.969	0.974	**0.971**	0.982
	QLSTM	**0.993**	**0.986**	**0.973**	**0.927**	**0.919**	0.923	0.858	**0.874**	**0.973**	**0.975**	**0.971**	**0.983**
Wuhan	SARIMA	0.858	0.703	0.862	0.913	0.901	0.928	0.933	0.916	0.956	0.896	0.896	0.904
	CNN	0.881	0.690	0.883	0.925	0.895	0.919	0.927	0.915	0.963	0.918	0.923	0.926
	RNN	0.911	0.752	**0.897**	0.938	0.917	0.936	0.940	**0.934**	0.966	**0.931**	0.929	0.924
	GRU	0.913	**0.756**	0.893	0.936	0.909	0.930	0.938	0.925	0.962	0.927	0.931	**0.930**
	LSTM	0.911	0.755	**0.897**	0.932	0.924	0.932	0.935	0.929	0.960	0.927	0.930	0.928
	QLSTM	**0.914**	0.737	0.894	**0.940**	**0.925**	**0.939**	**0.945**	**0.934**	**0.971**	0.927	**0.933**	0.922
Haikou	SARIMA	0.814	0.873	0.894	0.946	0.920	0.934	0.923	0.916	0.909	0.928	0.906	0.885
	CNN	0.838	0.893	0.911	0.950	0.931	0.931	0.918	0.917	0.909	0.929	0.921	0.894
	RNN	0.833	0.895	0.909	0.954	0.934	0.934	0.911	0.913	0.911	0.934	0.912	0.898
	GRU	0.835	0.891	0.906	0.952	0.934	0.942	0.926	0.920	0.915	0.938	0.919	0.901
	LSTM	0.846	0.898	0.909	**0.955**	0.936	0.942	**0.927**	0.922	**0.917**	**0.940**	0.919	0.898
	QLSTM	**0.848**	**0.900**	**0.915**	**0.955**	**0.939**	**0.945**	0.924	**0.925**	**0.917**	0.937	**0.927**	**0.905**

TABLE 6. Comparison of Two Papers

	Paper 1	Paper 2
Method	LSTM	QLSTM
Data	USA (Atlanta, New York and Hawaii)	China (Urumqi, Hohhot, Harbi, Wuhan and Haikou)
Time span	1 January 2013−31 December 2017	1 January 2016−31 December 2019
Metric	RMSE, MAE, MAPE, and R^2	RMSE, MAE, and R^2
Contrast model	ARIMA, SVR, BPNN, CNN and RNN	SARIMA, CNN, RNN, GRU, and LSTM
Experimental conditions	Three types of weather	Four seasons and 12 months

its variants have better processing capacity for time series. In RNN series models, the performance of the QLSTM model is better than that of other models. In Hainan, the QLSTM obtained 10 highest R^2, LSTM obtained four highest R^2. This is due to the tropical monsoon climate in Hainan, which has an obvious rainy season and less rainy season, leading to large fluctuations in solar radiation and reduced prediction accuracy of the model. Figs. 9 and 10 show the monthly values of RMSE and MAE. It can be seen from Fig. 9 that the RMSE of QLSTM has achieved the lowest value of 50 out of 60 groups of results. At the same time, it can be seen from Fig. 10 that the MAE value of QLSTM is the lowest in 59 groups of 60 results. All in all, the best prediction performance still belongs to the proposed hybrid QLSTM model irrespective of months and cities.

D. COMPARISON OF LSTM AND QLSTM

This article is a follow-up study based on the paper titled "An LSTM short-term solar irradiance forecasting under complicated weather conditions." Table 6 shows the comparison of the two papers. This article proposes a high-precision hybrid prediction model for solar irradiance based on VQC and LSTM networks. The proposed model embedded VQC in LSTM to iteratively optimize the weight parameters of four gates, namely, forgetting gate, input gate, cell state, and output gate, to improve the forecast accuracy. The performance of the proposed model is evaluated and compared with widely used models, including SARIMA, CNN, RNN, GRU, and LSTM, under different seasons and months using data from five solar radiation observatories in China. Results show that the proposed model significantly outperforms other models, with reductions in RMSE and MAE ranging from 3.4% to 28.9% and 10.7% to 28.1%, respectively, and improvements in R^2 ranging from 0.4% to 1.9%. The proposed model can enhance the security of grid operation by ensuring the scheduling and dispatching of electrical power and designing a PV-integrated energy management system. Overall, this article provides a promising approach for improving the accuracy of solar irradiance predictions.

However, that paper focuses on predicting solar irradiance under complicated weather conditions. The proposed approach improves the accuracy of predictions on cloudy days. This article introduces the use of a clearness index to classify the type of weather during data processing, which helps to improve the accuracy of predictions. The performance of different models, including BPNN and SVR, is compared, and the results show that the LSTM-based approach is more

accurate. The proposed approach is demonstrated to be generalizable across different regions through a cross-regional study. Overall, this article makes a valuable contribution to the field of PV forecasting methods and provides insights for future research in this area.

V. CONCLUSION

This article proposed a hybrid quantum LSTM model for one-hour-ahead solar irradiance prediction, which combines VQC and LSTM to obtain richer time-dependent information in meteorological and solar radiation data. Different meteorological data consisting of solar radiation, temperature, pressure, relative humidity, wind speed, cloud type, dew point, and solar zenith angle related to solar irradiance are considered to improve the prediction accuracy of the QLSTM model. The performance of the QLSTM model is evaluated based on the RMSE, MAE, and R^2 results and compared with other existing models such as SARIMA, CNN, RNN, GRU, and LSTM. The experimental results show that the annual average RMSE of the QLSTM model is 61.756 W/m^2, which is reduced by 10.7%, 13.9%, 8.1%, 3.8%, and 3.4%, respectively, compared with other models; the annual average MAE is 24.257 W/m^2, which is reduced by 28.1%, 28.9%, 24.1%, 12.2%, and 12.8%, respectively, compared with other models; the annual average R^2 is 0.946, which is improved by 1.5%, 1.9%, 1.2%, 0.4%, and 0.4%, respectively, compared with other models. Our work provides a reference for the application of quantum computing in the field of renewable energy. In the future, we will try to implement this predictive system in a NISQ computer. Generally, the implementation of quantum algorithms on NISQ computers can provide valuable insights into the behavior of quantum systems and help identify practical applications for these devices. However, the performance obtained may be limited by the noise and errors of the system, and achieving useful results may require significant optimization and error correction techniques.

REFERENCES

[1] J. D. Sachs et al., "Six transformations to achieve the sustainable development goals," *Nature Sustainability*, vol. 2, no. 9, pp. 805–814, 2019, doi: 10.1038/s41893-019-0352-9.

[2] S. Dunnett et al., "Harmonised global datasets of wind and solar farm locations and power," *Sci. Data*, vol. 7, no. 1, 2020, Art. no. 130, doi: 10.1038/s41597-020-0469-8.

[3] F. Wang et al., "A day-ahead PV power forecasting method based on LSTM-RNN model and time correlation modification under partial daily pattern prediction framework," *Energy Convers. Manage.*, vol. 212, 2020, Art. no. 112766, doi: 10.1016/j.enconman.2020.112766.

[4] Y. Yu et al., "Comparison of short-term solar irradiance forecasting methods when weather conditions are complicated," *J. Renewable Sustain. Energy*, vol. 10, no. 5, 2018, Art. no. 053501, doi: 10.1063/1.5041905.

[5] D. Yang et al., "Operational solar forecasting for grid integration: Standards, challenges, and outlook," *Sol. Energy*, vol. 224, pp. 930–937, 2021, doi: 10.1016/j.solener.2021.04.002.

[6] A. Colmenar-Santos et al., "Technical challenges for the optimum penetration of grid-connected photovoltaic systems: Spain as a case study," *Renewable Energy*, vol. 145, pp. 2296–2305, 2020, doi: 10.1016/j.renene.2019.07.118.

[7] L. Hernández-Callejo, S. Gallardo-Saavedra, and V. A. Alonso-Gómez, "review of photovoltaic systems: Design, operation and maintenance," *Sol. Energy*, vol. 188, pp. 426–440, 2019, doi: 10.1016/j.solener.2019.06.017.

[8] H. Sharadga, S. Hajimirza, and R. S. Balog, "Time series forecasting of solar power generation for large-scale photovoltaic plants," *Renewable Energy*, vol. 150, pp. 797–807, 2020, doi: 10.1016/j.renene.2019.12.131.

[9] A. Alfadda, S. Rahman, and M. Pipattanasomporn, "Solar irradiance forecast using aerosols measurements: A data driven approach," *Sol. Energy*, vol. 170, pp. 924–939, 2018, doi: 10.1016/j.solener.2018.05.089.

[10] Y. Hao and C. Tian, "A. novel two-stage forecasting model based on error factor and ensemble method for multi-step wind power forecasting," *Appl. Energy*, vol. 238, pp. 368–383, 2019, doi: 10.1016/j.apenergy.2019.01.063.

[11] M. López, C. Sans, S. Valero, and C. Senabre, "Empirical comparison of neural net- work and auto-regressive models in short-term load forecasting," *Energies*, vol. 11, 2018, Art. no. 2080, doi: 10.3390/en11082080.

[12] S. N. Singh and A. Mohapatra, "Repeated wavelet transform based ARIMA model for very short-term wind speed forecasting," *Renewable Energy*, vol. 136, pp. 758–768, 2019, doi: 10.1016/j.renene.2019.01.031.

[13] M. H. Alsharif, M. K. Younes, and J. Kim, "Time series ARIMA model for prediction of daily and monthly average global solar radiation: The case study of Seoul, South Korea," *Symmetry*, vol. 11, no. 2, 2019, Art. no. 240, doi: 10.3390/sym11020240.

[14] R. Basmadjian and A. Shaafieyoun, "ARIMA-based forecasts for the share of renewable energy sources: The case study of Germany," in *Proc. 3rd Int. Conf. Smart Grid Renewable Energy*, 2022, pp. 1–6, doi: 10.1109/SGRE53517.2022.9774082.

[15] S. Atique, S. Noureen, V. Roy, V. Subburaj, S. Bayne, and J. Macfie, "Forecasting of total daily solar energy generation using ARIMA: A case study," in *Proc. IEEE 9th Annu. Comput. Commun. Workshop Conf.*, 2019, pp. 0114–0119, doi: 10.1109/CCWC.2019.8666481.

[16] R. Basmadjian, A. Shaafieyoun, and S. Julka, "Day-ahead forecasting of the percentage of renewables based on time-series statistical methods," *Energies*, vol. 14, no. 21, 2021, Art. no. 7443, doi: 10.3390/en14217443.

[17] S. I. Vagropoulos, G. I. Chouliaras, E. G. Kardakos, C. K. Simoglou, and A. G. Bakirtzis, "Comparison of SARIMAX, SARIMA, modified SARIMA and ANN-based models for short-term PV generation forecasting," in *Proc. IEEE Int. Energy Conf.*, 2016, pp. 1–6, doi: 10.1109/ENERGYCON.2016.7514029.

[18] F. A. Eldali, T. M. Hansen, S. Suryanarayanan, and E. K. P. Chong, "Employing ARIMA models to improve wind power forecasts: A case study in ERCOT," in *Proc. North Amer. Power Symp.*, 2016, pp. 1–6, doi: 10.1109/NAPS.2016.7747861.

[19] A. Mellit and A. M. Pavan, "A 24-h forecast of solar irradiance using artificial neural network: Application for performance prediction of a grid-connected PV plant at Trieste, Italy," *Sol Energy*, vol. 84, pp. 807–21, 2010, doi: 10.1016/j.solener.2010.02.006.

[20] J. Shi, W-J Lee, Y. Liu, Y. Yang, and P. Wang, "Forecasting power output of photovoltaic systems based on weather classification and support vector machines," *IEEE Trans. Ind. Appl.*, vol. 48, pp. 1064–1069, May/Jun. 2012, doi: 10.1109/TIA.2012.2190816.

[21] S. Cao and J. Cao, "Forecast of solar irradiance using recurrent neural networks combined with wavelet analysis," *Appl. Thermal Eng.*, vol. 25, no. 2-3, pp. 161–172, 2005, doi: 10.1016/j.applthermaleng.2004.06.017.

[22] M. Aslam, J.-M Lee, H.-S Kim, S.-J Lee, and S. Hong, "Deep learning models for long-term solar radiation forecasting considering microgrid installation: A comparative study," *Energies*, vol. 13, no. 1, 2020, Art. no. 147, doi: 10.3390/en13010147.

[23] Y. Yu, J. Cao, and J. Zhu, "An LSTM short-term solar irradiance forecasting under complicated weather conditions," *IEEE Access*, vol. 7, pp. 145651–145666, 2019, doi: 10.1109/ACCESS.2019.2946057.

[24] X. Qing and Y. Niu, "Hourly day-ahead solar irradiance prediction using weather forecasts by LSTM," *Energy*, vol. 148, pp. 461–468, 2018, doi: 10.1016/j.energy.2018.01.177.

[25] O. Laib, M. T. Khadir, and L. Mihaylova, "Toward efficient energy systems based on natural gas consumption prediction with LSTM recurrent neural networks," *Energy*, vol. 177, pp. 530–542, 2019, doi: 10.1016/j.energy.2019.04.075.

[26] Y. Zhang, C. Qin, A. K. Srivastava, C. Jin, and R. K. Sharma, "Data-driven day-ahead PV estimation using autoencoder-LSTM and persistence model," *IEEE Trans. Ind. Appl.*, vol. 56, no. 6, pp. 7185–7192, Nov./Dec. 2020, doi: 10.1109/TIA.2020.3025742.

[27] K. Wang, X. Qi, and H. Liu, "Photovoltaic power forecasting based LSTM-convolutional network," *Energy*, vol. 189, 2019, Art. no. 116225, doi: 10.1016/j.energy.2019.116225.

[28] J. Preskill, "Quantum computing in the NISQ era and beyond," *Quantum*, vol. 2, 2018, Art. no. 79, doi: 10.22331/q-2018-08-06-79.

[29] M. Schuld et al., "Circuit-centric quantum classifiers," *Phys. Rev. A*, vol. 101, no. 3, 2020, Art. no. 032308, doi: 10.1103/PhysRevA.101.032308.

[30] B. T. Gard et al., "Efficient symmetry-preserving state preparation circuits for the variational quantum eigensolver algorithm," *npj Quantum Inf.*, vol. 2020, no. 3, Art. no. 032309, doi: 10.1103/PhysRevA.98.032309.

[31] I. Griol-Barres et al., "Variational quantum circuits for machine learning. An application for the detection of weak signals," *Appl. Sci.*, vol. 11, no. 14, 2021, Art. no. 6427, doi: 10.3390/app11146427.

[32] Z. He et al., "Variational quantum compiling with double Q-learning," *New J. Phys.*, vol. 23, no. 3, 2021, Art. no. 033002, doi: 10.1088/1367-2630/abe0ae.

[33] C. Bravo-Prieto et al., "Scaling of variational quantum circuit depth for condensed matter systems," *Quantum*, vol. 4, 2020, Art. no. 272, doi: 10.22331/q-2020-05-28-272.

[34] K. Mitarai et al., "Quantum circuit learning," *Phys. Rev. A*, vol. 98, no. 3, 2018, Art. no. 032309, doi: 10.1103/PhysRevA.98.032309.

[35] S. Y. C. Chen, C. H.-H. Yang, J. Qi, P. -Y. Chen, X. Ma, and H.-S. Goan, "Variational quantum circuits for deep reinforcement learning," *IEEE Access*, vol. 8, pp. 141007–141024, 2020, doi: 10.1109/ACCESS.2020.3010470.

[36] A. Giani and Z. Eldredge, "Quantum computing opportunities in renewable energy," *SN Comput. Sci.*, vol. 2, no. 5, 2021, Art. no. 393, doi: 10.1007/s42979-021-00786-3.

[37] M. Marquis, J. P. Kleissl, and C. F. Coimbra, "Energy meteorology: Solar and wind resourcing, forecasting, and integration II posters," in *Proc. AGU Fall Meeting 2019*, Aug. 2019.

[38] C. Wan, J. Zhao, Y. Song, Z. Xu, J. Lin, and Z. Hu, "Photovoltaic and solar power forecasting for smart grid energy management," *CSEE J. Power Energy Syst.*, vol. 1, no. 4, pp. 38–46, Dec. 2015, doi: 10.17775/CSEE-JPES.2015.00046.

[39] F. Gaitan, "Finding flows of a Navier-Stokes fluid through quantum computing," *npj Quant Inf.*, vol. 6, 2019, Art. no. 61, doi: 10.1038/s41534-020-00291-0.

[40] S. S. Bharadwaj and K. R. Sreenivasan, "Quantum computation of fluid dynamics," 2020, *arXiv:2007.09147*.

[41] J. Yepez, *Quantum Computation of Fluid Dynamics, Quantum Computing and Quantum Communications*. Berlin, Germany: Springer; 1999. pp. 34–60, doi: 10.1007/3-540-49208-9_3.

[42] N. Ray, T. Banerjee, B. Nadiga, and S. Karra, "Towards solving the Navier-Stokes equation on quantum computers," 2019, *arXiv:1904.09033*.

[43] F. Wang, C. Liu, and Y. Xu, "Analyzing population density disparity in China with GIS-automated regionalization: The Hu line revisited," *Chin. Geographical Sci.*, vol. 29, no. 4, pp. 541–552, 2019, doi: 10.1007/s11769-019-1054-y.

[44] S. Wang and H. Chen, "A novel deep learning method for the classification of power quality disturbances using deep convolutional neural network," *Appl. Energy*, vol. 235, pp. 1126–1140, 2019, doi: 10.1016/j.apenergy.2018.09.160.

[45] J. Lago, F. De Ridder, and B. De Schutter, "Forecasting spot electricity prices: Deep learning approaches and empirical comparison of traditional algorithms," *Appl. Energy*, vol. 221, pp. 386–405, 2018, doi: 10.1016/j.apenergy.2018.02.069.

[46] L. Palagi et al., "Machine learning for the prediction of the dynamic behavior of a small scale ORC system," *Energy*, vol. 166, pp. 72–82, 2019, doi: 10.1016/j.energy.2018.10.059.